

Construction of Active Site in a Sintered Copper–Ceria Nanorod Catalyst

Wen-Zhu Yu,^{†,||} Wei-Wei Wang,^{†,||} Shan-Qing Li,[‡] Xin-Pu Fu,[†] Xu Wang,[§] Ke Wu,^{⊥,#} Rui Si,^{*,§} Chao Ma,^{||,Ⓜ} Chun-Jiang Jia,^{*,†,Ⓜ} and Chun-Hua Yan^{*,⊥,#,Ⓜ}

[†]Key Laboratory for Colloid and Interface Chemistry, Key Laboratory of Special Aggregated Materials, School of Chemistry and Chemical Engineering, Shandong University, Jinan 250100, China

[§]Shanghai Synchrotron Radiation Facility, Shanghai Institute of Applied Physics, Chinese Academy of Sciences, Shanghai 201204, China

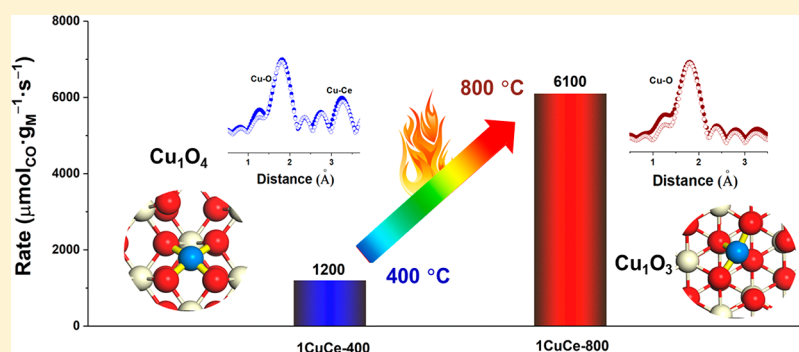
[‡]Department of Chemistry and Materials Engineering, Chizhou University, Chizhou 247000, China

^{||}College of Materials Science and Engineering, Hunan University, Changsha 410082, China

[⊥]Beijing National Laboratory for Molecular Sciences, State Key Lab of Rare Earth Materials Chemistry and Applications, PKU-HKU Joint Lab in Rare Earth Materials and Bioinorganic Chemistry, Peking University, Beijing 100871, China

[#]College of Chemistry and Chemical Engineering, Lanzhou University, Lanzhou 730000, China

Supporting Information



ABSTRACT: The construction of stable active site in nanocatalysts is of great importance but is a challenge in heterogeneous catalysis. Unexpectedly, coordination-unsaturated and atomically dispersed copper species were constructed and stabilized in a sintered copper–ceria catalyst through air-calcination at 800 °C. This sintered copper–ceria catalyst showed a very high activity for CO oxidation with a CO consumption rate of $6100 \mu\text{mol}_{\text{CO}} \cdot \text{g}_{\text{Cu}}^{-1} \cdot \text{s}^{-1}$ at 120 °C, which was at least 20 times that of other reported copper catalysts. Additionally, the excellent long-term stability was unbroken under the harsh cycled reaction conditions. Based on a comprehensive structural characterization and mechanistic study, the copper atoms with unsaturated coordination in the form of Cu_1O_3 were identified to be the sole active site, at which both CO and O_2 molecules were activated, thus inducing remarkable CO oxidation activity with a very low copper loading (1 wt %).

INTRODUCTION

In practical heterogeneous catalysis, the problems of contact and interaction between reactants and complex solid surfaces cause barriers to the design and preparation of high-performance nanocatalysts.^{1,2} Crucial to addressing this challenge are coordinatively unsaturated centers, which act as sites for the activation of reactant molecules at the interface between active metals and their supports, that however are confined to mild conditions.^{3–7} Inescapably, the active site in nanocatalysts are apt to sinter on-stream.⁸ On one hand, sintering is always a serious problem that causes many negative changes to catalysts, including the collapse of texture, the decrease in surface area, and especially, the loss of active site.^{9,10} On the other hand, sintering induces a surface

reconstruction of the support that can change the coordination structure of certain atoms,^{9,11} through which the inactive coordination-saturated atoms can be activated. Therefore, sintering establishes ways to construct new active site, although this approach seems difficult to achieve.

The CO oxidation reaction ($\text{CO} + \frac{1}{2} \text{O}_2 = \text{CO}_2$) is a well-known model reaction for fundamental catalysis study as well as a crucial process to resolve environmental pollution derived from many origins, especially automobile exhaust.^{12,13} The temperature range of exhausts is so wide that it represents a serious problem, which demands that the catalysts must

Received: May 21, 2019

Published: October 13, 2019

possess a good activity at low temperatures and remain structurally stable at high temperatures to meet the challenge.¹⁴ Although noble metals^{15–17} have exhibited the most promising catalytic activity to eliminate CO, their applications are restricted by cost and sintering at high temperatures. Recently, ceria was chosen to anchor Pt by calcination at 800 °C to obtain stable single atoms, which partly overcame the sintering of the metal, but the reactivity was still unsatisfactory.^{18–20} In contrast, copper is an alternative candidate, especially when supported on ceria at high loadings (>5 wt %), that has been intensively studied for CO elimination and utilization.^{21–24} However, the coexistence of a high activity and admirable thermal stability is not yet available in copper–ceria catalysts, which limits the material's application in practical catalysis.²⁵ Meanwhile, the atomic structure of the active site in copper–ceria catalysts is still unclear and remains under debate.^{26–28} Clustered copper oxide,²⁶ copper species strongly interacting with the ceria,²⁷ and even large CuO particles²⁸ have all been proven as active for CO oxidation; however, the contributions of isolated copper atoms with unsaturated coordination to the activity in catalyzing CO oxidation remain to be explored.

Here, we report the construction of atomically dispersed and coordination-unsaturated copper species, which were in the form of Cu₁O₃, as the sole active site in sintered copper–ceria catalysts, for which the advantages of the high activity of coordinately unsaturated centers and the excellent stability of a sintered support matrix were combined. The complex showed a remarkable CO oxidation rate of 6100 μmol_{CO}·g_{Cu}⁻¹·s⁻¹ at 120 °C, which was at least 20 times that of any other reported copper-based catalyst. Combining a kinetic study and theoretical calculations, we identified the Cu₁O₃ species as the sole active site, at which effective CO adsorption and O₂ activation occurred competitively.

EXPERIMENTAL METHODS

Catalyst Preparation. *Preparation of Ceria Nanorods.* All the chemicals were of analytical grade without further purification. The ceria nanorods were prepared by a hydrothermal method per the previous report.²⁹ First, Ce(NO₃)₃·6H₂O (1.30 g to 20 mL of Millipore water) was added to an aqueous NaOH solution (14.40 g to 40 mL of Millipore water) under vigorous stirring. After 0.5 h, the suspension was transferred into a Teflon bottle, followed by sealing in a stainless-steel autoclave. The assembly was subsequently transferred into a temperature-controlled electric oven and was subjected to hydrothermal treatment at 100 °C for 24 h. Finally, the fresh precipitates were separated by centrifugation, washed, and then dried at 60 °C overnight for standby application.

Preparation of Copper–Ceria Catalyst. The catalysts were prepared by a deposition–precipitation method, according to previous reports.^{26,30} In a typical preparation, 0.5 g of ceria powder was added to 25 mL of Millipore water at room temperature and under vigorous stirring for 0.5 h. A certain amount of Cu(NO₃)₂·3H₂O was added to the above suspension dropwise. The pH value of the solution was kept ca. 9 by the assistance of Na₂CO₃ during the whole course. The precipitates were further aged at room temperature for 1 h, and then, they were purified by vacuum filtration with Millipore water (1 L) at room temperature. Finally, the product was dried at 75 °C overnight (named as 1CuCe-dry) and then calcined in static air at different temperatures for 4 h. In our report, the copper–ceria samples were denoted 1CuCe-*y*, where 1 is the copper loading in weight percent and *y* is the calcination temperature, for example, 1CuCe-800 (the calcination temperature was 800 °C).

Preparation of Reference Catalysts. The gold–ceria catalyst (named as 1AuCe-NR) was synthesized according to the colloidal deposition method.³¹ First, a polyvinyl alcohol (PVA) solution and 2

mL of a 0.0125 mol·L⁻¹ HAuCl₄ solution were added to 48 mL of Millipore water under vigorous stirring. Then, 1.3 mL of NaBH₄ aqueous solution (0.1 mol·L⁻¹) was injected rapidly, and 0.5 g of ceria nanorods was immediately added. Then, the solids were gathered by filtration and washed with Millipore water. Finally, the sample was dried at 60 °C overnight, followed by calcination at 300 °C for 4 h. The referenced copper–ceria catalyst was prepared by the coprecipitation method, and Na₂CO₃ (0.1 mol·L⁻¹) was used as precipitant.³² Certain amounts of Cu(NO₃)₂·3H₂O and Ce(NO₃)₃·6H₂O were dissolved in 25 mL of Millipore water under vigorous stirring. The pH value of the solution was adjusted to ca. 9 by the adding the Na₂CO₃ solution. After the same treatment as that used for 1CuCe-400 and 1CuCe-800, we obtained four catalysts with different copper loadings (1CuCe-CP-400, 1CuCe-CP-800, 10CuCe-CP-400, and 10CuCe-CP-800). The ceria nanoparticles were prepared per the previous report.²⁶ With the assistance of cetyltrimethylammonium bromide (CTAB), Ce(NO₃)₃·6H₂O was precipitated by NaOH until the pH was approximately 9. After aging at 90 °C for 3 h, the suspension was centrifuged, washed, and dried. The catalysts were prepared by the same way as that for 1CuCe-400 and 1CuCe-800 and were named 1CuCe-NP-400 and 1CuCe-NP-800.

Characterization of Catalysts. *Transmission Electron Microscopy (TEM).* TEM and high-resolution TEM (HRTEM) were conducted on a FEI Tecnai G² F20 microscope operating at 200 kV. The high-angle annular dark-field scanning transmission electron microscopy (HAADF-STEM) images were obtained on a JEOL ARM200F microscope equipped with a probe-forming spherical-aberration corrector and Gatan image filter (Quantum 965).

X-ray Diffraction (XRD). The XRD pattern was performed on a PANalytical X'pert3 powder diffractometer (40 kV, 40 mA) using Cu Kα radiation (λ = 0.154 18 nm). The powder samples were placed inside a quartz-glass holder, and the diffraction angles ranged from 10° to 90°.

X-ray Photoelectron Spectroscopy (XPS). XPS characterization was carried out on an Axi Ultra X-ray imaging photoelectron spectrometer with an Al Kα radiator, and the vacuum in the analysis chamber was maintained at approximately 10⁻⁹ mbar. The binding energy was calibrated by means of the C 1s peak energy at 284.8 eV.

Inductively Coupled Plasma Atomic Emission Spectroscopy (ICP-AES). The copper loadings of all catalysts were detected by ICP-AES on an IRIS Intrepid II XSP instrument (Thermo Electron Corporation).

The N₂ Adsorption–Desorption Measurements. The N₂ adsorption–desorption measurements proceeded on a Builder SSA-4200 surface area analyzer at 77 K after completing the activation of the copper–ceria catalysts at 200 °C for 6 h under vacuum. The Brunauer–Emmett–Teller (BET) specific surface area was calculated from these data.

CO Titration. The CO titration was performed on a mass spectrum (LC-D200M, TILON) instrument. First, 100 mg of catalyst (20–40 mesh) was pretreated by O₂ at 300 °C for 0.5 h and then purged with He until the O₂ physically adsorbed on the catalyst was eliminated. Then, CO was introduced to the catalyst while the temperature was held at 100 °C. The CO (*m/z* = 28) and CO₂ signals (*m/z* = 44) were detected.

Temperature Program Reduction by Hydrogen (H₂-TPR). The hydrogen temperature program reduction was conducted on a Builder PCSA-1000 instrument. First, 30 mg of catalyst (20–40 mesh) was pretreated by O₂ at 300 °C for 0.5 h and then purged with Ar. The final test was carried out in 5% H₂/Ar (30 mL·min⁻¹) from room temperature to 400 °C (ramping rate: 10 °C·min⁻¹).

Raman Test. All the Raman spectra were collected by using a LabRAM HR800 spectrometer (Horiba Jobin Yvon) with laser excitation at 473 nm. The samples were attached to a glass slide, and Raman shifts were acquired from 200 to 1000 cm⁻¹ with a spectral resolution of 2 cm⁻¹.

X-ray Absorption Fine Structure (XAFS). The *ex situ* XAFS spectra of the Cu K-edge (*E*₀ = 8979 eV) for fresh and used catalysts were collected at the BL14W1 beamline at Shanghai Synchrotron Radiation Facility (SSRF), which was operated at 3.5 GeV in “top-up” mode

with a constant current of 260 mA. The XAFS data were collected in fluorescence mode with a seven-element Ge solid-state detector. The energy was calibrated according to the absorption edge of pure Cu foil. Athena and Artemis codes were used to extract the data and fit the profiles. For the X-ray absorption near-edge structure (XANES) analysis, the experimental absorption coefficients as a function of energy, $\mu(E)$, were processed by background subtraction and normalization procedures and were reported as “normalized absorption”. For the extended X-ray absorption fine structure (EXAFS) section, the Fourier transformed (FT) data in R space were analyzed by applying the first-shell approximation for the Cu–O or Cu–Ce shell. The passive electron factors, S_0^2 , were determined by fitting the experimental Cu foil data and fixing the Cu–Cu coordination number (CN) at 12; then, the factors remained fixed for further analysis of the measured samples. The parameters describing the electronic properties (e.g., the correction to the photoelectron energy origin, E_0) and local structure environment including the CN, bond distance (R), and Debye–Waller factor (σ^2) around the absorbing atoms were allowed to vary during the fit process.

In Situ Diffuse Reflectance Infrared Fourier Transform Spectroscopy (DRIFTS). In situ DRIFTS spectra were obtained using a Bruker Vertex 70 FTIR spectrometer fitted with an MCT detector. The DRIFTS cell (Harrick) was equipped with CaF_2 windows and a heating cartridge that allowed samples to be heated. An electrocontrol quick switching system was used to rapidly change the various gases without an ultrabit dead volume through a six-way valve. Approximately 40 mg of catalyst was tested in the reaction cell. Typically, an acquisition time of 30 s at a resolution of 4 cm^{-1} was used for the spectrum collection. The intensities were evaluated in Kubelka–Munk units, and the background was obtained using a spectrum recorded in pure N_2 at the same temperature as above. In pulse mode, the gas was introduced to the catalyst by an order of 2% CO/N_2 – N_2 –2% O_2/N_2 – N_2 , and the spectra were gathered during N_2 purging. In switching mode, the gas was led to the catalyst in the ranking of 2% CO – N_2 –2% CO –2% O_2 . Each gas was maintained for 0.5 h to play its role thoroughly. For exploring the states of the catalyst during the reaction, the reaction gas (1% CO , 20% O_2 , and 79% N_2) passed over the catalyst at different temperatures and stayed at each temperature for 0.5 h.

Density Functional Theory (DFT) Calculations. The heterogeneous catalysis simulations were carried out using the Vienna ab Initio simulation package.^{33–36} The Perdew–Burke–Ernzerhof (PBE) exchange–correlation functional and the projector augmented-wave (PAW) pseudopotential were applied to geometry optimizations.^{36–38} The cutoff energy for the plane wave basis was set to 400 eV. The convergence threshold of the electronic self-consistency was specified as 0.01 MeV, and the total energy change of the whole catalyst system between two ionic relaxation steps was designated as less than 0.02 eV. To accurately describe the Ce 4f orbitals, a Hubbard U term (DFT+ U) was involved in the first-principle computations, and the value of U was scaled to 4.5 eV, in accordance with previous research.^{39–41} The cleaved CeO_2 {111} surface comprised a nine-layer slab (Ce 3 layers and O 6 layers; the bottom 3 layers were fixed) as well as a vacuum layer of 15 Å. As to the CeO_2 {110} surface, two of the total six layers were restricted. The Brillouin zone of the constructed ($3 \times 3 \times 1$) supercell of the {111} surface was sampled with the k -points ($2 \times 2 \times 1$). For simulating catalyzing behaviors, the crystal defect was constructed by removing one molecule of ceria and replacing it with one molecule of CuO. With regard to the {110} surface, all approaches followed the same way except that a ($2 \times 3 \times 1$) supercell was created.

Catalytic Tests and Kinetics Measurement. *Catalytic Performance.* The CO oxidation test for the copper–ceria catalysts was conducted using a fixed-bed flow reactor under a gas mixture of 1% CO , 20% O_2 , and 79% N_2 at a flow rate of $67\text{ mL}\cdot\text{min}^{-1}$. Initially, 50 mg of catalyst (20–40 mesh) was used for the light-off test from room temperature to $300\text{ }^\circ\text{C}$ (ramping rate: $5\text{ }^\circ\text{C}\cdot\text{min}^{-1}$) and for the steady-state test at $100\text{ }^\circ\text{C}$. Prior to the measurement, the samples were pretreated in synthetic air (21% O_2 and 79% N_2) at $300\text{ }^\circ\text{C}$ for

0.5 h. The concentrations of CO and CO_2 in the outlet gas were quantified online by a nondispersive IR spectroscopy (Gasboard-3500, Wuhan Sifang Company, Wuhan, China).

$$X_{\text{CO}} = \frac{(n_{\text{CO}}^{\text{inlet}} - n_{\text{CO}}^{\text{outlet}})}{n_{\text{CO}}^{\text{inlet}}} \times 100\%$$

The CO conversion is defined as the following formula: The $n_{(\text{CO})}^{\text{inlet}}$ and $n_{(\text{CO})}^{\text{outlet}}$ indicated the concentrations of the CO analyzed by nondispersive IR spectroscopy of the incoming and effluent gases, respectively.

Apparent Activation Energy (E_a) and Reaction Order. For both catalysts, the E_a and reaction order were measured with the same reactor for catalytic performance described above. An appropriate amount of catalyst diluted with SiO_2 was used, and the experiments were carried out by changing the temperature and gas flow rate, with the conversion within the kinetic regime.

RESULTS AND DISCUSSION

Structure and Catalytic Performance. We prepared the copper–ceria catalyst by depositing a very small amount of copper (1 wt %) on the ceria nanorods, which was followed by a calcination treatment at $800\text{ }^\circ\text{C}$, with the sample named as 1CuCe-800. This catalyst showed a significant superiority in catalyzing CO oxidation in that its CO consumption rate reached $6100\text{ }\mu\text{mol}_{\text{CO}}\cdot\text{g}_{\text{Cu}}^{-1}\cdot\text{s}^{-1}$ at $120\text{ }^\circ\text{C}$, which was at least 20 times that of the other copper-based catalysts in the references.^{23,42} Especially, this value was even 30 times that of the activated single-atom Pt/ CeO_2 S catalyst (Figure 1a).¹⁹ Generally, the practical utility of highly effective catalysts has been limited by the low coverage of active species dispersed on

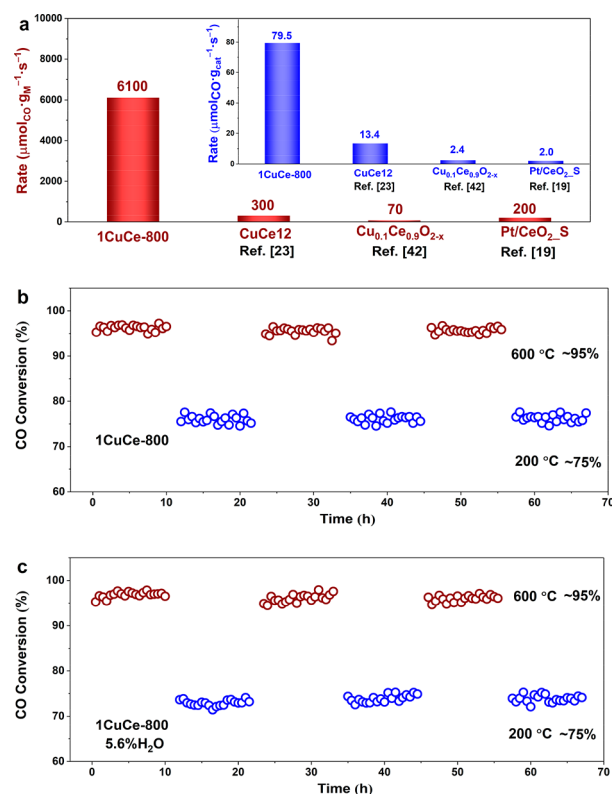


Figure 1. (a) Comparison of CO conversion rates over 1CuCe-800, CuCe12, $\text{Cu}_{0.1}\text{Ce}_{0.9}\text{O}_{2-x}$ and Pt/ CeO_2 S catalysts at $120\text{ }^\circ\text{C}$ (detail in Table 1). The cyclic stability of the 1CuCe-800 catalyst alternately tested at 600 and $200\text{ }^\circ\text{C}$ (5 mg of catalyst, GHSV: $240\,000\text{ mL}\cdot\text{g}_{\text{cat}}^{-1}\cdot\text{h}^{-1}$) (b) without water and (c) with water.

Table 1. Summary of Relevant Activities Tested at 120 °C^a

catalyst	loading	conversion	gas composition	GHSV	rate 1	rate 2	ref
1CuCe-800	1.3	77.0	1% CO–20% O ₂ –79% N ₂	402 000	38.4	3000	this study
1CuCe-800	1.3	12.7	1% CO–20% O ₂ –79% N ₂	1 200 000	18.9	1500	this study
1CuCe-800	1.3	8.9	3% CO–5% O ₂ –92% N ₂	2 400 000	79.5	6100	this study
1CuCe-400	1.2	34.0	1% CO–20% O ₂ –79% N ₂	80 400	3.4	300	this study
1CuCe-400	1.2	12.8	1% CO–20% O ₂ –79% N ₂	600 000	9.5	800	this study
1CuCe-400	1.2	6.6	3% CO–5% O ₂ –92% N ₂	600 000	14.7	1200	this study
1CuCe-CP-400	1.0	6.0	1% CO–20% O ₂ –79% N ₂	80 400	0.6	100	this study
1CuCe-CP-800	1.0	3.0	1% CO–20% O ₂ –79% N ₂	80 400	0.3	50	this study
10CuCe-CP-400	10.0	17.5	1% CO–20% O ₂ –79% N ₂	80 400	1.7	20	this study
10CuCe-CP-800	10.0	3.0	1% CO–20% O ₂ –79% N ₂	80 400	0.3	5	this study
CuCe12	4.4	90.0	1% CO–1% O ₂ –98% N ₂	120 000	13.4	300	23
CeO ₂ –CuO	3.3	80.0	1% CO–10% O ₂ –89% N ₂	60 000	6.0	200	24
Cu _{0.1} Ce _{0.9} O _{2-x}	3.7	25.0	1% CO–2.5% O ₂ –96.5% Ar	78,000	2.4	100	42
Pt/CeO ₂ _S	1.0	20.0	0.4% CO–10% O ₂ –89.6% Ar	200 000	2.0	200	19
PdO/Ce _{1-x} Pd _x O _{2-δ}		50.0	0.95% CO–1.75% O ₂ –97.3% N ₂	12 000	0.7		44

^aThe units of each column are (loading) wt %, (conversion) %, (GHSV) mL·g_{cat}⁻¹·h⁻¹, (rate 1) μmol·g_{cat}⁻¹·s⁻¹, and (rate 2) μmol·g_M⁻¹·s⁻¹.

supports.⁴³ However, here, the activity of the 1CuCe-800 catalyst even presented a reaction rate per overall catalyst mass 6 times that of the reference catalysts (the inset of Figure 1a and Table 1). Additionally, this 1CuCe-800 catalyst possessed remarkable cyclic stability under harsh reaction conditions in which the temperature periodically increased to 600 °C and then decreased to 200 °C (Figure 1b). This endurance under the high-temperature condition was significantly better than that of the ceria-supported gold catalyst, as well as pure ceria (Figure S1). Even in the presence of moisture, no deactivation was experimentally found (Figure 1c) when compared with the activity in a dry environment (Figure 1b). Moreover, when the gas hourly space velocity (GHSV) reached a very high value of approximately ~240 000 mL·g_{cat}⁻¹·h⁻¹, 1CuCe-800 showed an 80% CO conversion at approximately 100 °C (Figure S2). This result preceded that of the reported Pt/CeO₂_S catalyst, which just began to catalyze CO to CO₂ at the same temperature.¹⁹ The properties of 1CuCe-800 bring good news for governing exhaust because it provides promising possibilities to practical applications thanks to its endurance under conditions of variable temperature, moisture, and high gas hourly space velocity.

After the cyclic test shown in Figure 1b and the light-off test in Figure S2, the morphology of 1CuCe-800 was characterized, and the results are presented in Figure 2a, b, and c. The used catalysts exhibited no differences from the fresh one (Figure S3a). However, the sample underwent sintering, as evident when compared with its precursors not subjected to the high-temperature calcination (named as 1CuCe-dry, Figure S3b). This difference is also evident from the sharp peaks of the XRD patterns in Figure S4a and from the serious decrease in surface area from 107 m²·g⁻¹ to 32 m²·g⁻¹ (Table S1). The lengths of the nanorods became very short (approximately 50 nm) and were sintered to show irregular shapes. Interestingly, no aggregation of copper occurred in the used 1CuCe-800 catalyst, let alone in the fresh sample, as indicated by the elemental mapping results (Figure 2d). The high dispersion of copper was also confirmed by the absence of XRD peaks relevant to any Cu/Cu₂O/CuO phases for both the fresh and used samples (Figure S4b), as well as by the EXAFS results shown later.

To pursue the origin of the outstanding catalytic performance, we further explored the influence of the calcination

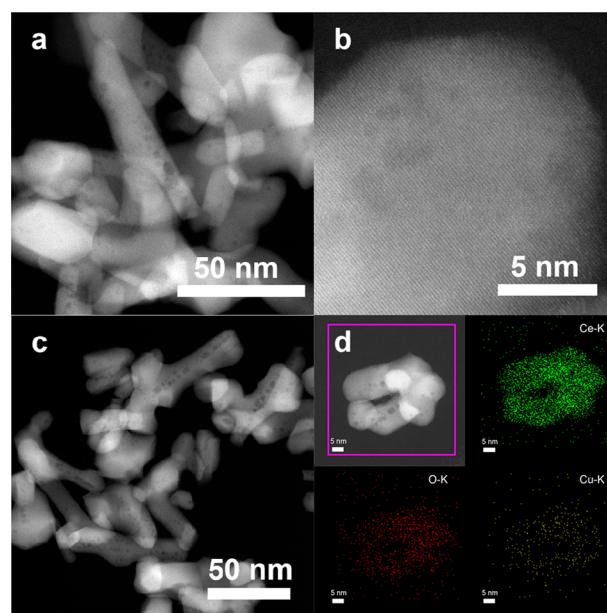


Figure 2. (a and b) Aberration-corrected HAADF-STEM images of the 1CuCe-800 catalyst after the periodic stability test between 600 and 200 °C. (c) Aberration-corrected HAADF-STEM images and (d) EDS elemental mapping images of the used (after the light-off test) 1CuCe-800 catalyst.

temperature (Figure S5a). A lower temperature (at 400 °C) treatment resulted in only an approximately 10% conversion of CO at 100 °C, while 1CuCe-800 yielded a nearly full conversion. Moreover, a higher temperature (at 1000 °C) treatment caused severe activity loss (Figure 3a). During the stability test, these catalysts showed no deactivation but expressed evident differences in their abilities to eliminate CO (Figure S5b). In view of such differences, the redox properties of the catalysts were determined by temperature-programmed reduction using hydrogen (H₂-TPR). In Figure 3b and Figure S5c, the reduction peak at 165 °C, with a small shoulder at or around 155 °C, appeared for 1CuCe-800. With 1CuCe-400, a broad reduction peak at 165–400 °C was observed. While for 1CuCe-1000, the Cu species began to be reduced over 300 °C. Such differences induced clear variations in activity, which was also reflected by the *E*_a value (Figure S5d). Based on the H₂-

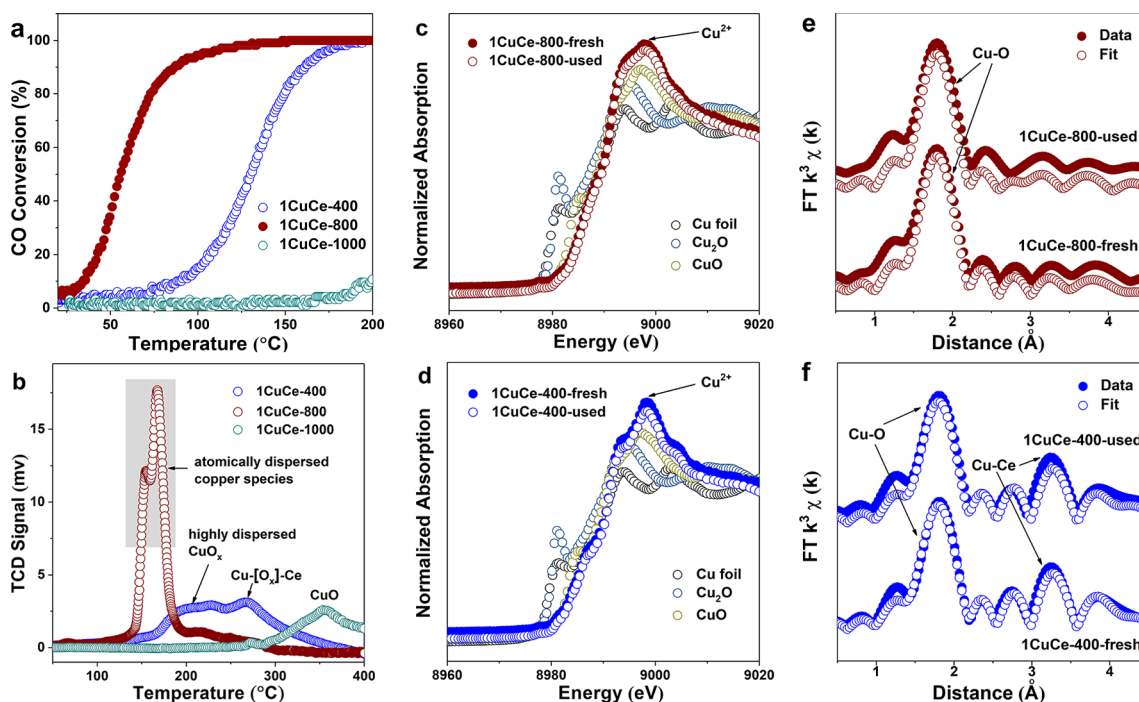


Figure 3. (a) Light-off test of CO oxidation ($[\text{CO}] = 1\%$, $[\text{O}_2] = 20\%$ and balanced with N_2 at a GHSV of $80\,400\text{ mL}\cdot\text{g}_{\text{cat}}^{-1}\cdot\text{h}^{-1}$), (b) H_2 -TPR profiles over 1CuCe catalysts with different calcination temperatures. XANES spectra of (c) 1CuCe-800 and (d) 1CuCe-400. EXAFS spectra of (e) 1CuCe-800 and (f) 1CuCe-400.

TPR results, the copper interacted distinctly with the ceria after the heat treatment at various temperatures, which led to the different degrees of sintering for these samples (Figures S6 and S7). The optimized Cu-CeO₂ interaction that induced the remarkable activity for CO oxidation was obtained by a reasonable treatment at 800 °C.

Coordination Environments of Copper Atoms. To clarify the origin of such different interactions, the X-ray absorption fine structure (XAFS) technique (Figure 3c–f and Figure S8) was used. All the catalysts clearly demonstrated the prevailing presence of Cu(II), in both fresh and used samples. For 1CuCe-800, a main Cu–O shell ($R \approx 1.9\text{ \AA}$, CN ≈ 3.3) with a minor Cu–Ce contribution from Cu–[O_x]-Ce structures²⁶ ($R \approx 3.3\text{ \AA}$, CN ≈ 0.5) was determined. Therefore, the copper sites were atomically dispersed on ceria in both fresh and used samples (Figure 3e and Table S2).^{26,45} Different from 1CuCe-800, 1CuCe-400 possessed a main Cu–O shell ($R \approx 1.9\text{ \AA}$, CN ≈ 3.7) and an apparent Cu–Ce component, which was from the Cu–[O_x]-Ce structures²⁶ ($R \approx 3.3\text{ \AA}$, CN ≈ 2.7), verifying the presence of a strong interaction between copper and ceria (Figure 3f and Table S2). The copper species in 1CuCe-1000 aggregated as CuO particles, which corresponded well with the pure CuO reference. Combining the EXAFS results, we assigned all the reduction peaks in the H_2 -TPR profiles. The broad reduction peak from 165 to 400 °C for the 1CuCe-400 catalyst was attributed to highly dispersed CuO_x and the Cu–[O_x]-Ce structures.²⁶ For 1CuCe-800, the two adjacent sharp reduction peaks at temperatures below 200 °C were considered to be atomically dispersed copper species that weakly interacted with the ceria.

On the basis of the EXAFS fitting results, DFT calculations were performed to simulate the exact structure of the Cu atoms on the ceria surface. It has been reported that ceria nanorods treated at a high temperature were largely enclosed

by {111} facets—instead of the {110} surfaces—because of surface reconstruction.^{9,46} This result was also confirmed in our samples by HRTEM (Figure S6e). Therefore, a “CuO” unit was used to replace a “CeO₂” unit, ensuring electric neutrality on the surface of the CeO₂ {111} planes with the formation of terrace vacancies (more details in Figures S9–S11). The tricoordinated Cu₁O₃ species adhered to the terrace vacancies on the CeO₂ {111} were formed in this optimized configuration to simulate 1CuCe-800 (Figure 4a,b and Table S3), and its formation energy was -0.58 eV (Table S4). In this optimized configuration, the number of Cu–O bonds (ranging from 1.90 to 1.93 Å) was 3 in the first coordination shell of the

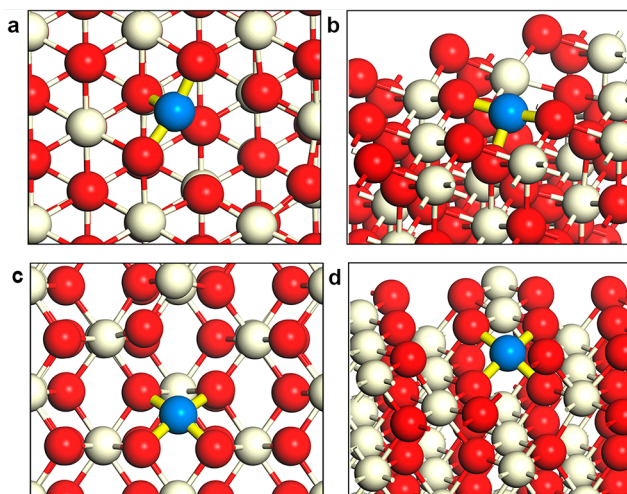


Figure 4. (a and b) Optimized structures of a copper atom on CeO₂ {111} and (c and d) optimized structures of a copper atom on CeO₂ {110} to simulate 1CuCe-800 and 1CuCe-400, respectively (blue: Cu, red: O, and white: Ce).

Cu atom, which was consistent with the coordination number of Cu in 1CuCe-800 being approximately 3.3 from the EXAFS fitting (Table S2). Commonly, the copper atoms in ceria possess a square planar configuration, bonding to four lattice oxygen atoms under the surface.⁴⁷ However, here, the atomically dispersed copper species in the sintered copper–ceria catalyst were indubitably determined to be coordinately unsaturated as Cu_1O_3 . Furthermore, the adsorption of one more O to Cu_1O_3 on CeO_2 {111} to form Cu_1O_4 , as given by $\text{CuO}/\text{Ce}_{26}\text{O}_{52} + \frac{1}{2}\text{O}_2 \rightarrow \text{CuO}/\text{Ce}_{26}\text{O}_{53}$ ($\Delta G = 0.87$ eV, 100 °C, and $p_{\text{O}_2} = 20$ kPa), would be thermodynamically unfavorable. Such a transformation would be forbidden even at 1000 °C (Table S5), indicating the sufficient stability of Cu_1O_3 on CeO_2 {111}. Analogously, an optimized configuration for 1CuCe-400 was also constructed. One “CuO” was introduced on the CeO_2 {110} planes with the formation energy being -1.76 eV because the ceria nanorods were largely enclosed by {110} planes when they were subjected to a low-temperature pretreatment,²⁹ which was also proven by HRTEM (Figure S6d). In this model, the copper atoms were linked to four oxygen atoms to form a square planar coordination structure with the Cu–O bond lengths ranging from 1.93 to 1.97 Å (Figure 4c,d), which was the same as that of copper on ceria {110} in another report.⁴⁸ The formation Gibbs free energy of an oxygen vacancy at the interface of Cu– CeO_2 {110} was calculated, as represented by this formula: $\text{CuO}/\text{Ce}_{26}\text{O}_{52} \rightarrow \text{CuO}/\text{Ce}_{26}\text{O}_{51} + \frac{1}{2}\text{O}_2$ ($\Delta G = 1.24$ eV, 100 °C, and $p_{\text{O}_2} = 20$ kPa). The positive reaction energy declared that Cu_1O_4 was not inclined to lose an O atom to form Cu_1O_3 on the CeO_2 {110}. This configuration matched well with that from the EXAFS fitting of the first shell structure of Cu atoms (Table S2). Of note is the presence of some differences between the EXAFS fitting and DFT calculation results for the second coordination shell of Cu atoms. In the optimized structure configuration of 1CuCe-800, with respect to the second coordination shell of the Cu atom, two long Cu–O–Ce bridge bonds with nearly the same Cu–Ce distances (approximately 4.00 Å) were present (Table S3); these features were only slightly related to the metal–support (Cu– CeO_2) interaction and could therefore be ignored. Meanwhile, two shorter Cu–O–Ce bonds, with the nearly the same Cu–Ce distances of approximately 3.11 Å, were formed and which contributed to the interaction between the Cu atom and the CeO_2 support. It is noted that the coordination number of Cu–Ce for the second shell of Cu atoms was 2 in the optimized model, while that value was only 0.5 for 1CuCe-800 based on the EXAFS fitting. Such a difference indicated that the copper atoms in 1CuCe-800 were structurally disordered, which was impossible to reflect in the optimized surface model. Similarly, for 1CuCe-400, four Cu–O–Ce bonds with distances ranging from 3.09 to 3.25 Å (Table S3) were obtained in this model; therefore, the coordination number of Cu atoms in the second shell was 4, which was slightly higher than that (2.5) for 1CuCe-400 obtained from the EXAFS fitting.

From the above, we proposed that the loss of the strong interaction between the copper and ceria was favorable to induce a better activity for CO oxidation. On this basis, a comparative experiment was designed and carried out. After calcining at 400 °C, the as-prepared copper–ceria sample was further treated to a high-temperature (at 800 °C) calcination. This sample was labeled as 1CuCe-400–800 and had almost identical characteristics to those of 1CuCe-800, including the

activity for CO oxidation, the coordination environments of copper atoms, and the redox properties (Figure 5). Therefore,

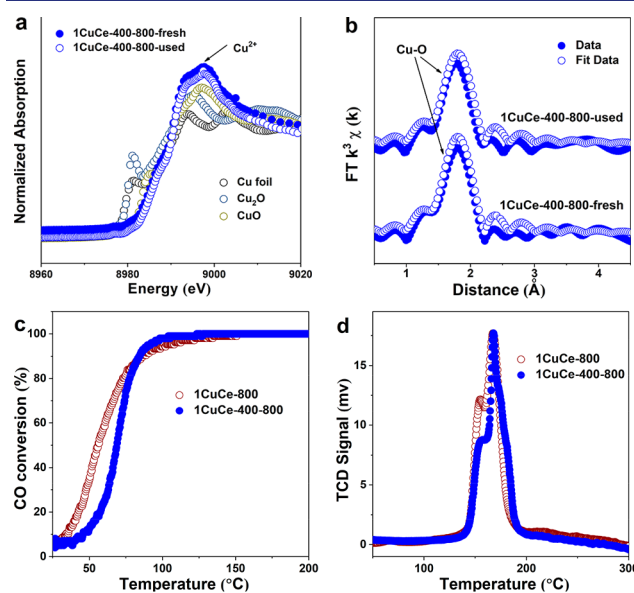


Figure 5. (a) XANES spectra, (b) EXAFS spectra, (c) the light-off test of CO oxidation, and (d) H_2 -TPR profiles of the 1CuCe-400–800 catalyst.

we concluded that reactive Cu_1O_3 species were formed by breaking the strong interaction between copper and ceria via a high-temperature treatment and accompanied by the surface reconstruction of ceria from the {110} to {111}, which was reflected by the cross-section morphology of the catalysts. The crucial role of the surface reconstruction exceeds our expectation because the activity enhancement did not happen when we used CeO_2 nanoparticles (Figures S12–S14) as supports with originally exposed {111} planes.^{26,32} The 1CuCe-NP sample sintered severely after 800 °C. Thus, 1CuCe-NP-800 yielded a worse activity than 1CuCe-NP-400.

Active Sites for CO Oxidation. After verifying the difference in the Cu sites for the distinctly treated catalysts, we wondered about the mechanistic insights into the active nature of the Cu_1O_3 structure. As we all know, CO adsorption is one of the crucial steps in CO oxidation. Therefore, the CO molecule was used as a probe to investigate the adsorption ability by DRIFTS (Figure 6a and Figures S15–S18), and a $\text{CO}-\text{N}_2-\text{CO}-\text{O}_2$ exchange experiment was conducted. A unimodal peak on 1CuCe-800 centered at 2112 cm^{-1} was observed, indicating the CO chemisorbed on Cu(I) species (CO–Cu(I)) (Figure 6a).^{49–51} Actually, the valence state of the copper in the copper–ceria catalysts was identified as Cu(II) by the *ex situ* XANES (Figure 3c,d). The Cu(II) in copper–ceria tended to be reduced even in vacuum, which was also proven by the XPS analysis (Figure S19).⁵² In the DRIFTS measurements, once CO interacted with the catalyst, the surface Cu(II) could be reduced to CO–Cu(I).⁵³ We found that the intensity of the CO–Cu(I) band (at $\sim 2110\text{ cm}^{-1}$) of 1CuCe-400 was approximately 20 times weaker than that of 1CuCe-800. In addition, a gaseous CO signal⁵⁴ appeared at $\sim 2165\text{ cm}^{-1}$ for 1CuCe-400 because of the inadequate adsorption. After the adsorption reached an equilibrium state at 120 °C, N_2 was introduced to liberate the active sites from CO, and the elimination of CO–Cu(I) was observed. In

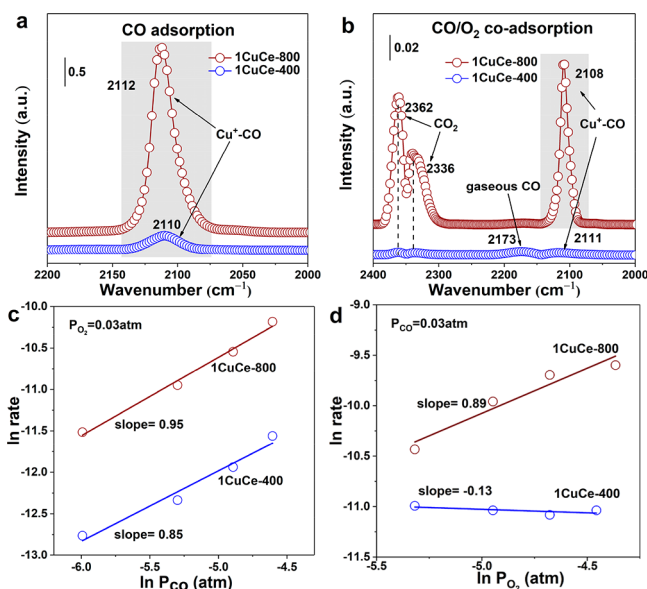


Figure 6. *In situ* DRIFTS spectra of 1CuCe-800 and 1CuCe-400 under (a) the CO adsorption condition and (b) the CO/O₂ coadsorption conditions at 120 °C. (c and d) Kinetic orders of the reactants (CO and O₂) for 1CuCe-800 and 1CuCe-400 at temperatures at 120 and 110 °C, respectively.

contrast, CO was introduced once again for 30 min, which was followed by the injection of O₂. This process produced CO₂ gas, the bands of which were centered at ~2362 and ~2334 cm⁻¹, indicating that CO-Cu(I) was rapidly oxidized by O₂ to form the CO₂ product.^{32,55} It is noteworthy that the ability of 1CuCe-400–800 to adsorb CO was identical to that of 1CuCe-800 (Figure S18), which corresponded to the similar structural characteristics between these two catalysts (Figure 6). The ability of 1CuCe-800 to adsorb CO was significantly improved compared with that of other copper–ceria catalysts, especially as was reflected by the pulse experiment (Figure S20). The large difference in the integrated intensities of CO adsorption and O₂ removal, which represented the activity, showed a clear gap between 1CuCe-800 and the other two catalysts during 15 cycles.

Apart from the CO adsorption, the activation of the O₂ molecule was also investigated. When we changed CO to a mixture of CO and O₂, 1CuCe-800 produced more CO₂ at different temperature gradients than did 1CuCe-400 (Figure 6b and Figure S21). Meanwhile, CO titration was used to assess the extent of possible participation by the reactive oxygen on the catalyst surface (Figure S22). After CO was introduced, the intensity of the CO₂ response for 1CuCe-800 was found to be slightly higher than that of 1CuCe-400 and 1CuCe-1000. However, such a difference could not explain the huge activity gap among these catalysts. At the same time, the oxygen vacancies that were favorable to activate O₂ were scantier in 1CuCe-800 reflected by the relative intensity ratio of I_D/I_{F2g} ⁵⁶ in Raman spectra (Figure S23a and Table S1). According to the CO titration and Raman spectra, the oxygen vacancies were confirmed as not crucial for 1CuCe-800, while it was not clear how O₂ was activated by 1CuCe-800 during the reaction. To clarify this scenario, the dependencies of the partial pressures of CO and O₂ on CO oxidation activity were demonstrated. The turnover rates for CO oxidation were proportional to the O₂ and CO pressures in 1CuCe-800 (Figure 6c,d and Figure S23b), giving kinetic orders of 0.95

and 0.89 for CO and O₂, respectively, proving the catalyst surface was not CO-saturated to impede O₂ adsorption.⁵⁷ In addition to a superior ability for CO adsorption, the enhanced activity of 1CuCe-800 was revealed to potentially be rooted in the activation of O₂ molecules on the tricoordinated Cu₁O₃ species competitively, since the unsaturated copper atoms were apt to search for small molecules to form a square planar configuration. In contrast, the measured CO and O₂ reaction orders for 1CuCe-400 under the same conditions were 0.85 and ~0 (−0.13), respectively. This result meant that O₂ was activated easily on ceria because of its adequate oxygen vacancies, although its reactivity was limited by the insufficient adsorption of CO molecules.

To acquire a deep insight into the reaction mechanism, DFT calculations for all the steps proposed in the CO oxidation were carried out (Figure 7a–c and Table S6). For 1CuCe-800,

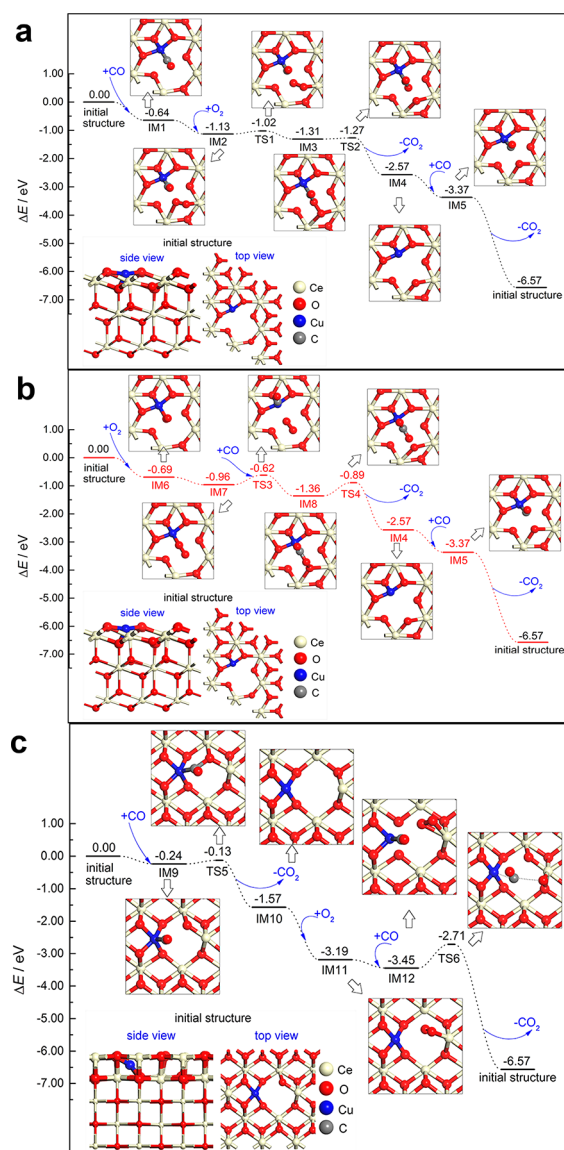


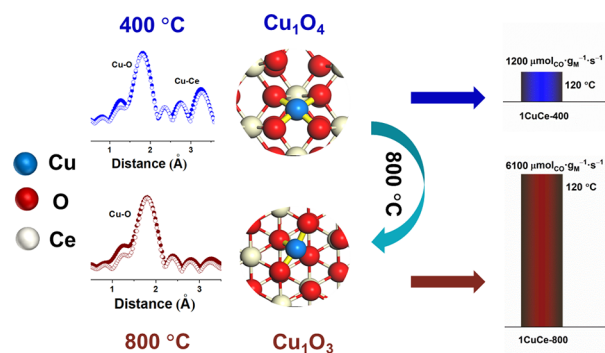
Figure 7. (a) CO adsorbed on coordination-unsaturated Cu₁O₃ as one first step and (b) O₂ adsorbed on the Cu₁O₃ as the other step for the reaction pathways over optimized structures of copper on CeO₂ {111} by the calculation tests. (c) CO adsorbed on coordination-unsaturated Cu₁O₄ as the first step over the optimized structures of copper on CeO₂ {110} by the calculation tests.

the surface adsorbed CO to form a four-coordination configuration first, and the corresponding adsorption energy was -0.64 eV, which was very close to the calculated binding energy value of CO on the Cu single atom catalyst (SAC) at the step site on CeO₂ in the previous report.⁵⁸ This step was followed by an adjustment in the adsorption configuration and then by the fast adsorption of O₂ on the surface of CeO₂ {111}. The residual oxygen atom after the producing CO₂ was liable to react with another CO to transform back to the stable configuration with a strong formation energy of -3.20 eV (Figure 7a). Alternatively, we started with O₂ adsorption on the copper atom and obtained an adsorption energy of -0.69 eV, which was almost the same as that for CO adsorption, together with the following steps (Figure 7b). Combined with the kinetics results, the data inferred that CO and O₂ could occupy the fourth coordination site of the unsaturated Cu₁O₃ species by similar competitiveness during reaction. The effective adsorption of CO and the facile activation of O₂ jointly resulted in the superior activity. For 1CuCe-400, because of the four-coordination structure of the copper atom, the adsorption of CO was substantially more difficult than on 1CuCe-800, where the adsorption energy was only -0.24 eV (Figure 7c). Further, when we tried to start with O₂ on the copper site as 1CuCe-800 did, the molecule could not adhere to such a copper species. In accordance with all the above results, the Cu₁O₃ activated both CO and O₂ molecules by itself and thus created the enhanced activity.

CONCLUSIONS

The pursuit of highly active and stable catalysts has always been difficult, although several efforts have been made to this effect. Herein, we accomplished a breakthrough in that we constructed stable and atomically dispersed Cu sites with unsaturated coordination in a sintered copper–ceria catalyst, as shown in Scheme 1. The Cu₁O₃ sites in 1CuCe-800 were

Scheme 1. Schematic Illustration of the Structure Evolution from Coordination-Saturated Active Sites in 1CuCe-400 to Coordination-Unsaturated Active Sites in 1CuCe-800.^a



^aWhite: Ce; red: O; and blue: Cu.

formed by breaking the strong interaction between copper and ceria. The transformation from Cu₁O₄ to Cu₁O₃ led to a greatly promoted CO oxidation activity, which was 20 times that of other copper-based catalysts, as well as a remarkable stability. The unsaturated Cu₁O₃ site activated both the CO and O₂ molecules simultaneously, thus inducing the greatly enhanced activity. The construction of unsaturated active site in the copper–ceria catalyst through sintering illustrates a new

route to design high-performance catalysts for heterogeneous catalysis.

ASSOCIATED CONTENT

Supporting Information

The Supporting Information is available free of charge on the ACS Publications website at DOI: 10.1021/jacs.9b05419.

Further experimental data, including XRD, DFT, characterization of the 1CuCe-NP samples, XPS, *in situ* DRIFTS, CO titration, Raman, and activity results (PDF)

AUTHOR INFORMATION

Corresponding Authors

*sirui@sinap.ac.cn

*jiacj@sdu.edu.cn

*yan@pku.edu.cn

ORCID

Chao Ma: 0000-0001-8599-9340

Chun-Jiang Jia: 0000-0002-4254-5100

Chun-Hua Yan: 0000-0002-0581-2951

Author Contributions

[†]W.-Z.Y. and W.-W.W. contributed equally.

Notes

The authors declare no competing financial interest.

ACKNOWLEDGMENTS

This work was financially supported by the Excellent Young Scientists Fund from National Science Foundation of China (NSFC) (grant no. 21622106), other projects from the NSFC (grant nos. 21331001, 21773288, 21805167, and 21771117), the Outstanding Scholar Fund from the Science Foundation of Shandong Province of China (grant no. JQ201703), the Doctoral Fund (grant no. ZR2018BB010) from the Science Foundation of Shandong Province of China, the Taishan Scholar Project of Shandong Province of China, the National Key Basic Research Program of China (grant no. 2017YFA0403402), and the Future Program for Young Scholars of Shandong University (grant no. 11190089964158). We thank the Center of Structural Characterizations and Property Measurements at Shandong University for their help with sample characterizations.

REFERENCES

- (1) Wu, Q. Q.; Jing, M. Z.; Wei, Y. C.; Zhao, Z.; Zhang, X. D.; Xiong, J.; Liu, J.; Song, W. Y.; Li, J. M. High-efficient catalysts of core-shell structured Pt@transition metal oxides (TMOs) supported on 3DOM-Al₂O₃ for soot oxidation: The effect of strong Pt-TMO interaction. *Appl. Catal., B* **2019**, *244*, 628–640.
- (2) Liu, T. Z.; Li, Q.; Xin, Y.; Zhang, Z. L.; Tang, X. F.; Zheng, L. R.; Gao, P. X. Quasi free K cations confined in hollandite-type tunnels for catalytic solid (catalyst)-solid (reactant) oxidation reactions. *Appl. Catal., B* **2018**, *232*, 108–116.
- (3) Kwak, J. H.; Hu, J. Z.; Mei, D. H.; Yi, C. W.; Kim, D. H.; Peden, C. H. F.; Allard, L. F.; Szanyi, J. Coordinatively unsaturated Al³⁺ centers as binding sites for active catalyst phases of platinum on -Al₂O₃. *Science* **2009**, *325*, 1670–1673.
- (4) Fu, Q.; Li, W. X.; Yao, Y. X.; Liu, H. Y.; Su, H. Y.; Ma, D.; Gu, X. K.; Chen, L. M.; Wang, Z.; Zhang, H.; Wang, B.; Bao, X. H. Interface-confined ferrous centers for catalytic oxidation. *Science* **2010**, *328*, 1141–1144.
- (5) Wang, F.; He, S.; Chen, H.; Wang, B.; Zheng, L. R.; Wei, M.; Evans, D. G.; Duan, X. Active site dependent reaction mechanism

over Ru/CeO₂ catalyst toward CO₂ methanation. *J. Am. Chem. Soc.* **2016**, *138*, 6298–6305.

(6) Kong, L. N.; Wei, W.; Zhao, Q. F.; Wang, J. Q.; Wan, Y. Active coordinatively unsaturated manganese Monoxide-containing mesoporous carbon catalyst in wet peroxide oxidation. *ACS Catal.* **2012**, *2*, 2577–2586.

(7) Yang, P. F.; Pan, J. H.; Liu, Y. N.; Zhang, X. Y.; Feng, J. T.; Hong, S.; Li, D. Q. Insight into the role of unsaturated coordination O_{2c}-Ti_{5c}-O_{2c} sites on selective glycerol oxidation over AuPt/TiO₂ catalysts. *ACS Catal.* **2019**, *9*, 188–199.

(8) Carter, J. H.; Liu, X.; He, Q.; Althahban, S.; Nowicka, E.; Freakley, S. J.; Niu, L. W.; Morgan, D. J.; Li, Y. W.; Niemantsverdriet, J. W.; Golunski, S.; Kiely, C. J.; Hutchings, G. J. Activation and deactivation of gold/ceria–zirconia in the low-temperature water–gas shift reaction. *Angew. Chem., Int. Ed.* **2017**, *56*, 16037–16041.

(9) Ta, N.; Liu, J. Y.; Chenna, S.; Crozier, P. A.; Li, Y.; Chen, A. L.; Shen, W. J. Stabilized gold nanoparticles on ceria nanorods by strong interfacial anchoring. *J. Am. Chem. Soc.* **2012**, *134*, 20585–20588.

(10) Slavinskaya, E. M.; Stadnichenko, A. I.; Muravyov, V. V.; Kardash, T. Y.; Derevyannikova, E. A.; Zaikovskii, V. I.; Stonkus, O. A.; Lapin, I. N.; Svetlichnyi, V. A.; Boronin, A. I. Transformation of a Pt–CeO₂ mechanical mixture of pulsed-laser-ablated nanoparticles to a highly active catalyst for carbon monoxide oxidation. *ChemCatChem* **2018**, *10*, 2232–2247.

(11) Aneggi, E.; Wiaterski, D.; de Leitenburg, C.; Llorca, J.; Trovarelli, A. Shape-dependent activity of ceria in soot combustion. *ACS Catal.* **2014**, *4*, 172–181.

(12) Liu, W.; Flytzani-Stephanopoulos, M. Total oxidation of carbon monoxide and methane over transition metal-fluorite oxide composite catalysts. *J. Catal.* **1995**, *153*, 304–316.

(13) Wan, H. Q.; Li, D.; Dai, Y.; Hu, Y. H.; Zhang, Y. H.; Liu, L. J.; Zhao, B.; Liu, B.; Sun, K. Q.; Dong, L.; Chen, Y. Effect of CO pretreatment on the performance of CuO/CeO₂/γ-Al₂O₃ catalysts in CO+O₂ reactions. *Appl. Catal., A* **2009**, *360*, 26–32.

(14) Kašpar, J.; Fornasiero, P.; Hickey, N. Automotive catalytic converters: current status and some perspectives. *Catal. Today* **2003**, *77*, 419–449.

(15) Rodriguez, J. A.; Ma, S.; Liu, P.; Hrbek, J.; Evans, J.; Pérez, M. Activity of CeO_x and TiO_x nanoparticles grown on Au (111) in the water-gas shift reaction. *Science* **2007**, *318*, 1757–1760.

(16) Hu, Z.; Liu, X. F.; Meng, D. M.; Guo, Y.; Guo, Y. L.; Lu, G. Z. Effect of ceria crystal plane on the physicochemical and catalytic properties of Pd/ceria for CO and propane oxidation. *ACS Catal.* **2016**, *6*, 2265–2279.

(17) Jia, C. J.; Liu, Y.; Bongard, H.; Schüth, F. Very low temperature CO oxidation over colloiddally deposited gold nanoparticles on Mg(OH)₂ and MgO. *J. Am. Chem. Soc.* **2010**, *132*, 1520–1522.

(18) Jones, J.; Xiong, H. F.; DeLaRiva, A. T.; Peterson, E. J.; Pham, H.; Challa, S. R.; Qi, G. S.; Oh, S.; Wiebenga, M. H.; Hernández, X. I. P.; Wang, Y.; Datye, A. K. Thermally stable single-atom platinum-on-ceria catalysts via atom trapping. *Science* **2016**, *353*, 150–154.

(19) Nie, L.; Mei, D. H.; Xiong, H. F.; Peng, B.; Ren, Z. B.; Hernández, X. I. P.; DeLaRiva, A.; Wang, M.; Engelhard, M. H.; Kovarik, L.; Datye, A. K.; Wang, Y. Activation of surface lattice oxygen in single-atom Pt/CeO₂ for low-temperature CO oxidation. *Science* **2017**, *358*, 1419–1423.

(20) Kunwar, D.; Zhou, S. L.; DeLaRiva, A.; Peterson, E. J.; Xiong, H. F.; Hernández, X. I. P.; Purdy, S. C.; Veen, R. T.; Brongersma, H. H.; Miller, J. T.; Hashiguchi, H.; Kovarik, L.; Lin, S.; Guo, H.; Wang, Y.; Datye, A. K. Stabilizing high metal loadings of thermally stable platinum single atoms on an industrial catalyst support. *ACS Catal.* **2019**, *9*, 3978–3990.

(21) Li, Y.; Fu, Q.; Flytzani-Stephanopoulos, M. Low-temperature water-gas shift reaction over Cu- and Ni-loaded cerium oxide catalysts. *Appl. Catal., B* **2000**, *27*, 179–191.

(22) Rodriguez, J. A.; Graciani, J.; Evans, J.; Park, J. B.; Yang, F.; Stacchiola, D.; Senanayake, S. D.; Ma, S. G.; Pérez, M.; Liu, P.; Sanz, J. F.; Hrbek, J. Water-Gas shift reaction on a highly active inverse

CeO_x/Cu(111) catalyst: unique role of ceria nanoparticles. *Angew. Chem., Int. Ed.* **2009**, *48*, 8047–8050.

(23) Luo, M. F.; Ma, J. M.; Lu, J. Q.; Song, Y. P.; Wang, Y. J. High-surface area CuO–CeO₂ catalysts prepared by a surfactant-templated method for low-temperature CO oxidation. *J. Catal.* **2007**, *246*, 52–59.

(24) Chen, G. Z.; Xu, Q. H.; Yang, Y.; Li, C. C.; Huang, T. Z.; Sun, G. X.; Zhang, S. X.; Ma, D. L.; Li, X. Facile and mild strategy to construct mesoporous CeO₂-CuO nanorods with enhanced catalytic activity toward CO oxidation. *ACS Appl. Mater. Interfaces* **2015**, *7*, 23538–23544.

(25) Fu, Q.; Saltsburg, H.; Flytzani-Stephanopoulos, M. Active nonmetallic Au and Pt species on ceria-based water-gas shift catalysts. *Science* **2003**, *301*, 935–938.

(26) Wang, W. W.; Yu, W. Z.; Du, P. P.; Xu, H.; Jin, Z.; Si, R.; Ma, C.; Shi, S.; Jia, C. J.; Yan, C. H. Crystal plane effect of ceria on supported copper oxide cluster catalyst for CO oxidation: importance of metal-support interaction. *ACS Catal.* **2017**, *7*, 1313–1329.

(27) Chen, A. L.; Yu, X. J.; Zhou, Y.; Miao, S.; Li, Y.; Kuld, S.; Sehested, J.; Liu, J. Y.; Aoki, T.; Hong, S.; Camellone, M. F.; Fabris, S.; Ning, J.; Jin, C. C.; Yang, C. W.; Nefedov, A.; Wöll, C.; Wang, Y. M.; Shen, W. J. Structure of the catalytically active copper–ceria interfacial perimeter. *Nature Catal.* **2019**, *2*, 334–341.

(28) Gamarra, D.; Munuera, G.; Hungria, A. B.; García, M. F.; Conesa, J. C.; Midgley, P. A.; Wang, X. Q.; Hanson, J. C.; Rodríguez, J. A.; Arias, A. M. Structure-activity relationship in nanostructured copper-ceria-based preferential CO oxidation catalysts. *J. Phys. Chem. C* **2007**, *111*, 11026–11038.

(29) Mai, H. X.; Sun, L. D.; Zhang, Y. W.; Si, R.; Feng, W.; Zhang, H. P.; Liu, H. C.; Yan, C. H. Shape-selective synthesis and oxygen storage behavior of ceria nanopolyhedra, nanorods, and nanocubes. *J. Phys. Chem. B* **2005**, *109*, 24380–24385.

(30) Si, R.; Raitano, J.; Yi, N.; Zhang, L. H.; Chan, S. W.; Stephanopoulos, M. F. Structure sensitivity of the low-temperature water-gas shift reaction on Cu–CeO₂ catalysts. *Catal. Today* **2012**, *180*, 68–80.

(31) Guo, L. W.; Du, P. P.; Fu, X. P.; Ma, C.; Zeng, J.; Si, R.; Huang, Y. Y.; Jia, C. J.; Zhang, Y. W.; Yan, C. H. Contributions of distinct gold species to catalytic reactivity for carbon monoxide oxidation. *Nat. Commun.* **2016**, *7*, 13481.

(32) Qi, L.; Yu, Q.; Dai, Y.; Tang, C. J.; Liu, L. J.; Zhang, H. L.; Gao, F.; Dong, L.; Chen, Y. Influence of cerium precursors on the structure and reducibility of mesoporous CuO–CeO₂ catalysts for CO oxidation. *Appl. Catal., B* **2012**, *119–120*, 308–320.

(33) Kresse, G.; Hafner, J. Ab initio molecular dynamics for liquid metals. *Phys. Rev. B: Condens. Matter Mater. Phys.* **1993**, *47*, 558–561.

(34) Kresse, G.; Furthmüller, J. Efficient iterative schemes for ab initio total-energy calculations using a plane-wave basis set. *Phys. Rev. B: Condens. Matter Mater. Phys.* **1996**, *54*, 11169–11186.

(35) Kresse, G.; Hafner, J. Ab initio molecular-dynamics simulation of the liquid-metal-amorphous-semiconductor transition in germanium. *Phys. Rev. B: Condens. Matter Mater. Phys.* **1994**, *49*, 14251–14269.

(36) Kresse, G.; Joubert, D. From ultrasoft pseudopotentials to the projector augmented-wave method. *Phys. Rev. B: Condens. Matter Mater. Phys.* **1999**, *59*, 1758–1775.

(37) Perdew, J. P.; Burke, K.; Ernzerhof, M. Generalized gradient approximation made simple. *Phys. Rev. Lett.* **1996**, *77*, 3865–3868.

(38) Blöchl, P. E. Projector augmented-wave method. *Phys. Rev. B: Condens. Matter Mater. Phys.* **1994**, *50*, 17953–17979.

(39) Saito, M.; Roberts, C. A.; Ling, C. DFT+U study of the adsorption and oxidation of an iron oxide cluster on CeO₂ support. *J. Phys. Chem. C* **2015**, *119*, 17202–17208.

(40) Liu, Y. L.; Li, H. Y.; Yu, J.; Mao, D. S.; Lu, G. Z. Electronic storage capacity of ceria: role of peroxide in Aux supported on CeO₂ (111) facet and CO adsorption. *Phys. Chem. Chem. Phys.* **2015**, *17*, 27758–27768.

(41) Zhang, J.; Gong, X. Q.; Lu, G. Z. Catalytic activities of CeO₂ (110)–2 × 1 reconstructed surface. *Surf. Sci.* **2015**, *632*, 164–173.

(42) Elias, J. S.; Risch, M.; Giordano, L.; Mansour, A. N.; Shao-Horn, Y. Structure, bonding, and catalytic activity of monodisperse, transition-metal-substituted CeO₂ nanoparticles. *J. Am. Chem. Soc.* **2014**, *136*, 17193–17200.

(43) Wang, A. Q.; Li, J.; Zhang, T. Heterogeneous single-atom catalysis. *Nat. Rev. Chem.* **2018**, *2*, 65–81.

(44) Meng, L.; Lin, J. J.; Pu, Z. Y.; Luo, L. F.; Jia, A. P.; Huang, W. X.; Luo, M. F.; Lu, J. Q. Identification of active sites for CO and CH₄ oxidation over PdO/Ce_{1-x}Pd_xO_{2-δ} catalysts. *Appl. Catal., B* **2012**, *119–120*, 117–122.

(45) Wang, Y. F.; Chen, Z.; Han, P.; Du, Y. H.; Gu, Z. X.; Xu, X.; Zheng, G. F. Single-atomic Cu with multiple oxygen vacancies on ceria for electrocatalytic CO₂ reduction to CH₄. *ACS Catal.* **2018**, *8*, 7113–7119.

(46) Huang, W. X.; Gao, Y. X. Morphology-dependent surface chemistry and catalysis of CeO₂ nanocrystals. *Catal. Sci. Technol.* **2014**, *4*, 3772–3784.

(47) Carey, J. J.; Nolan, M. Dissociative adsorption of methane on the Cu and Zn doped (111) surface of CeO₂. *Appl. Catal., B* **2016**, *197*, 324–336.

(48) Chutia, A.; Gibson, E. K.; Farrow, M. R.; Wells, P. P.; Scanlon, D. O.; Dimitratos, N.; Willock, D. J.; Catlow, C. A. The adsorption of Cu on the CeO₂ (110) surface. *Phys. Chem. Chem. Phys.* **2017**, *19*, 27191–27203.

(49) Zhou, K. B.; Wang, X.; Sun, X. M.; Peng, Q.; Li, Y. D. Enhanced catalytic activity of ceria nanorods from well-defined reactive crystal planes. *J. Catal.* **2005**, *229*, 206–212.

(50) Morales, F.; Smit, E. D.; Groot, F. M. F. D.; Visser, T.; Weckhuysen, B. M. Effects of manganese oxide promoter on the CO and H₂ adsorption properties of titania-supported cobalt Fischer–Tropsch catalysts. *J. Catal.* **2007**, *246*, 91–99.

(51) Elias, J. S.; Stoerzinger, K. A.; Hong, W. T.; Risch, M.; Giordano, L.; Mansour, A. N.; Shao-Horn, Y. *In situ* spectroscopy and mechanistic insights into CO oxidation on transition-metal-substituted ceria nanoparticles. *ACS Catal.* **2017**, *7*, 6843–6857.

(52) Zhang, X.; Zhu, X. B.; Lin, L. L.; Yao, S. Y.; Zhang, M. T.; Liu, X.; Wang, X. P.; Li, Y. W.; Shi, C.; Ma, D. Highly dispersed copper over β-Mo₂C as an efficient and stable catalyst for the reverse water gas shift (RWGS) reaction. *ACS Catal.* **2017**, *7*, 912–918.

(53) Elias, J. S.; Artrith, N.; Bugnet, M.; Giordano, L.; Botton, G. A.; Kolpak, A. M.; Shao-Horn, Y. Elucidating the nature of the active phase in copper/ceria catalysts for CO oxidation. *ACS Catal.* **2016**, *6*, 1675–1679.

(54) Wan, H. Q.; Wang, Z.; Zhu, J.; Li, X. W.; Liu, B.; Gao, F.; Dong, L.; Chen, Y. Influence of CO pretreatment on the activities of CuOII-Al₂O₃ catalysts in CO+O₂ reaction. *Appl. Catal., B* **2008**, *79*, 254–261.

(55) Green, I. X.; Tang, W. J.; Neurock, M.; Yates, J. T., Jr. Spectroscopic observation of dual catalytic sites during oxidation of CO on a Au/TiO₂ catalyst. *Science* **2011**, *333*, 736–739.

(56) Wu, Z. L.; Li, M. J.; Howe, J.; Meyer, H. M.; Overbury, S. H. Overbury, probing defect sites on CeO₂ nanocrystals with well-defined surface planes by Raman spectroscopy and O₂ adsorption. *Langmuir* **2010**, *26* (21), 16595–16606.

(57) Lu, Y. B.; Wang, J. M.; Yu, L.; Kovarik, L.; Zhang, X. W.; Hoffman, A. S.; Gallo, A.; Bare, S. R.; Sokaras, D.; Kroll, T.; Dagle, V.; Xin, H. L.; Karim, A. M. Identification of the active complex for CO oxidation over single-atom Ir-on-MgAl₂O₄ catalysts. *Nature Catal.* **2019**, *2*, 149–156.

(58) Wan, Q.; Wei, F. F.; Wang, Y. Q.; Wang, F. T.; Zhou, L. S.; Lin, S.; Xie, D. Q.; Guo, H. Single atom detachment from Cu clusters, and diffusion and trapping on CeO₂(111): implications in Ostwald ripening and atomic redispersion. *Nanoscale* **2018**, *10*, 17893–17901.